Space-Time Analysis of the Flow-Induced Vibration of a Solid Containing an Embedded Cylindrical Shell

Andrew J. Hull
Bruce M. Abraham
Submarine Sonar Department

19960221 079

Naval Undersea Warfare Center Division
Newport, Rhode Island

PREFACE

Reviewed and Approved: 18 December 1995

R. J. Martin
Acting Head, Submarine Sonar Department

REPORT DOCUMENTATION PAGE

Public reporting burden for this collection of information is estimated to average 1 hour per response, including the time for reviewing instructions, searching existing data sources, gathering and maintaining the data needed, and completing and reviewing the collection of information. Send comments regarding this burden estimate or any other aspect of this collection of information, including suggestions for reducing this burden, to Washington Headquarters Services, Directorate for information Operations and Reports, 1215 Jefferson Davis Highway, Suite 1204, Arlington, VA 22202-4302, and to the Office of Management and Budget, Paperwork Reduction Project (0704-0188), Washington, DC 20503.

1. AGENCY USE ONLY (Leave Blank)	2. REPORT DATE 18 December 1995	3. REPORT TYPE AND DATES COVERED Final

4. TITLE AND SUBTITLE	5. FUNDING NUMBERS
Space-Time Analysis of the Flow-Induced Vibration of a Solid Containing an Embedded Cylindrical Shell	

6. AUTHOR(S)

Andrew J. Hull and Bruce M. Abraham

7. PERFORMING ORGANIZATION NAME(S) AND ADDRESS(ES)	8. PERFORMING ORGANIZATION REPORT NUMBER
Naval Undersea Warfare Center Detachment New London New London, Connecticut 06320	TR 11,073

9. SPONSORING/MONITORING AGENCY NAME(S) AND ADDRESS(ES)	10. SPONSORING/MONITORING AGENCY REPORT NUMBER
Office of Naval Research 800 North Quincy Street Arlington, VA 22217	

11. SUPPLEMENTARY NOTES

12a. DISTRIBUTION/AVAILABILITY STATEMENT	12b. DISTRIBUTION CODE
Approved for public release; distribution is unlimited.	

13. ABSTRACT (Maximum 200 words)

This report develops a model of a viscoelastic solid that contains an embedded cylindrical shell through which fluid flows at low Mach number. The model output corresponds to the displacement that a beamformed, steered array of sensors would measure in wavenumber and frequency. The solid and the shell are modeled using elasticity equations of isotropic mediums. The fluid is modeled with two pressure terms: one that represents the acoustic pressure field and one that represents the normal forces of the turbulent boundary layer on the inner wall of the cylindrical shell. The fluid equations are coupled to the solid equations by conservation of momentum. The spatial (or wavenumber) response of the array and the array elements are also included in the model. All the model terms are assembled in an integral equation and numerically evaluated at various frequencies. The work is verified with an experiment in which gravity-fed water is passed through a piece of surgical tubing that is contained in the block. Displacement measurements of the free surface of the block are made with an eight-element array, and the results are compared to the theoretical model. It is shown that the model and the experiment are in good agreement.

14. SUBJECT TERMS	15. NUMBER OF PAGES
Elastic Medium, Embedded Cylindrical Shell, Flow-Induced Vibration, Space-Time Analysis, Turbulent Energy, Viscoelastic Solid	45
	16. PRICE CODE

17. SECURITY CLASSIFICATION OF REPORT	18. SECURITY CLASSIFICATION OF THIS PAGE	19. SECURITY CLASSIFICATION OF ABSTRACT	20. LIMITATION OF ABSTRACT
UNCLASSIFIED	UNCLASSIFIED	UNCLASSIFIED	SAR

NSN 7540-01-280-5500

TABLE OF CONTENTS

LIST OF ILLUSTRATIONS

LIST OF TABLES

SPACE-TIME ANALYSIS OF THE FLOW-INDUCED VIBRATION OF A SOLID CONTAINING AN EMBEDDED CYLINDRICAL SHELL

1. INTRODUCTION

The analysis of solid bodies with embedded cylindrical shells that contain transported fluids is not only pertinent to such mechanical systems as buried steam pipes, sewers, and heat exchangers, but also to biological systems, such as the arteries of the human body. The response of the solid body is dependent on the forces that the transported fluid exert on the surrounding medium. These forces typically cause wave motion in the medium, which, in turn, creates a displacement. Understanding the response of the medium is particularly important when the displacement and wave motion have undesirable effects. The response of a free surface of the medium may also be used to detect and localize the source (energy) emissions. The work documented in this report develops the theory and provides the experimental data to support detection and localization of flow in an unblocked shell surrounded by a lossy medium. Although this type of detection may be useful to surveyors trying to locate buried pipes, its primary intent is to locate partially blocked coronary arteries in humans.

In section 2, a model of a solid with an embedded tube containing a moving fluid is derived based on the wavenumber (space) and frequency (time) content of the wave motion. The model is evaluated at the surface of the solid, which corresponds to the position of a beamformed, linear array. The model is developed using the equations of elasticity in cylindrical coordinates coupled to a line source that represents the fluid. The medium is modeled as a semi-infinite solid that admits propagating shear and compressional wave energy. The filtering effects of the array and sensors are also included in the model.

In section 3, the closed-form solution of the model is compared to experimental data for validation. The experiment consists of a solid Hexcel 195-RE urethane block that contains an embedded surgical tube (figure 1). This block is an isotropic solid free of bone, tissue, and

other biological substances whose behavior cannot be easily resolved. The tube has an inner radius of 0.00159 m (1/16 in.), which is the approximate size of a human coronary artery. The distance from the surface of the solid to the tube is 0.0191 m (3/4 in.), which is approximately the minimum distance from a location on the third intercostal space to the nearest coronary artery in a human chest (Norton, 1995). Water is gravity fed into the surgical tube from a holding tank and captured below the block in a calibrated flask (figure 2). This technique permits measurement of the flow velocity. The moving fluid transmits a relatively small normal force into the embedded tube, which, in turn, transmits energy into the solid. This energy propagates to the surface of the block, primarily in the form of shear waves where it produces a local displacement.

The data in this experiment were collected with an eight-element array (figure 3) designed to detect the extremely small displacements that are typical of experiments with a low-level energy source. Each element of the array consists of a piece of stiff plastic mounted on a strip of polyvinylidene fluoride (PVDF). The PVDF is a piezoelectric polymer that acts as a strain gage when the plastic is displaced. Array technology improves the signal-to-noise ratio over single-point measurements and provides directionality to the detection process.

In section 4, the dynamic behavior of the model is discussed, and the differences between the model and the experimental data are examined.

The model and experiment developed here allow a controlled laboratory setting in which array technology is used to conduct tests of arterial flow. This effort provides a foundation for future investigations that would address the vibration of shells that include partial blockages, nonisotropic blocks, and focused optimal processing (beamforming) detection techniques.

Top View

Surgical Tube

0.276 m

Side View

0.0508 m

0.156 m

Front View

Surgical Tube

0.0191 m

0.0984 m
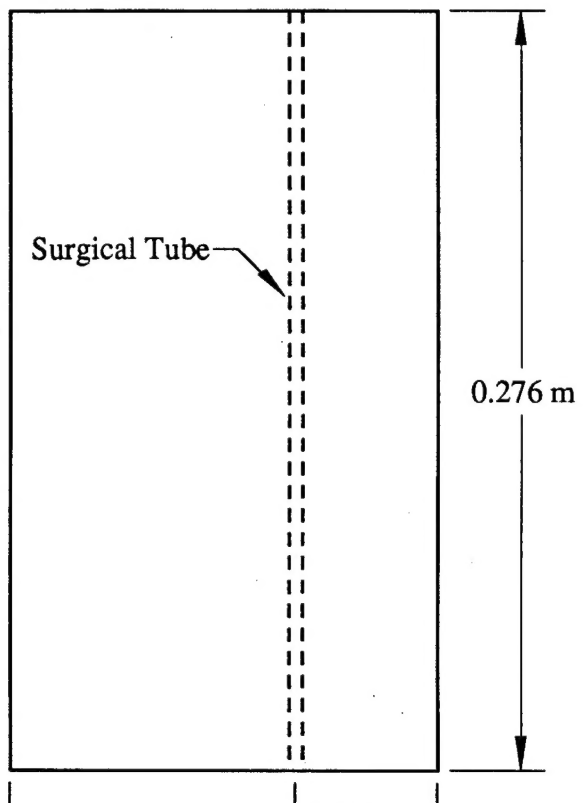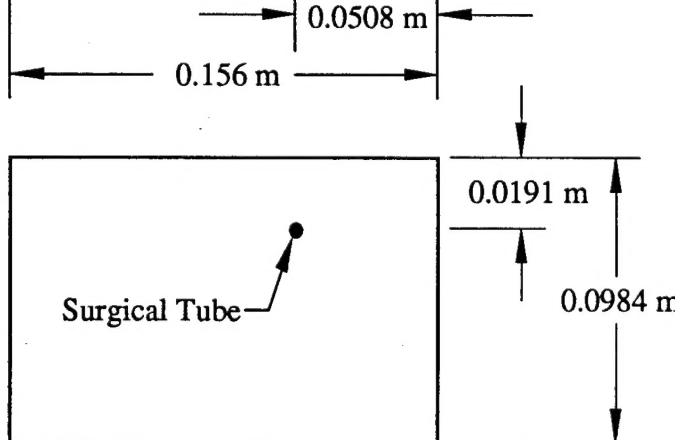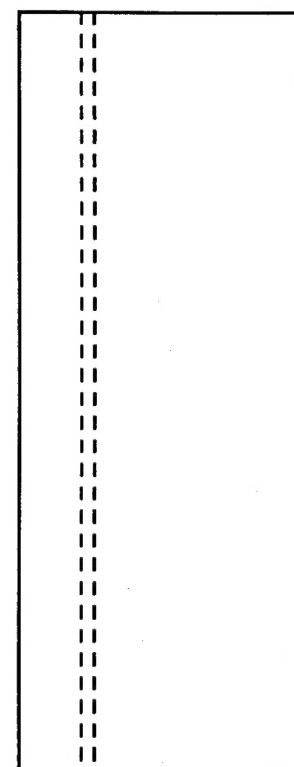
Scale: 1 to 2.72

Figure 1. Urethane Block With Embedded Surgical Tube
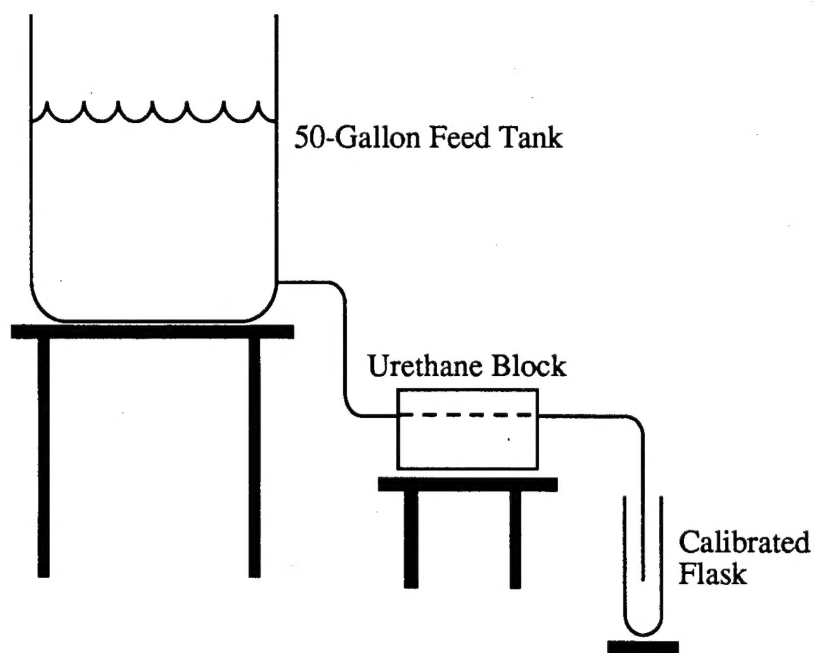
Figure 2. Laboratory Configuration

Bottom View

Front View

Element 2
Element 4
Element 6
Element 8

Element 1
Element 3
Element 5
Element 7

0.0127 m

0.0445 m

0.102 m

Measurement Axis

Contact Pads

Side View

Actual Size
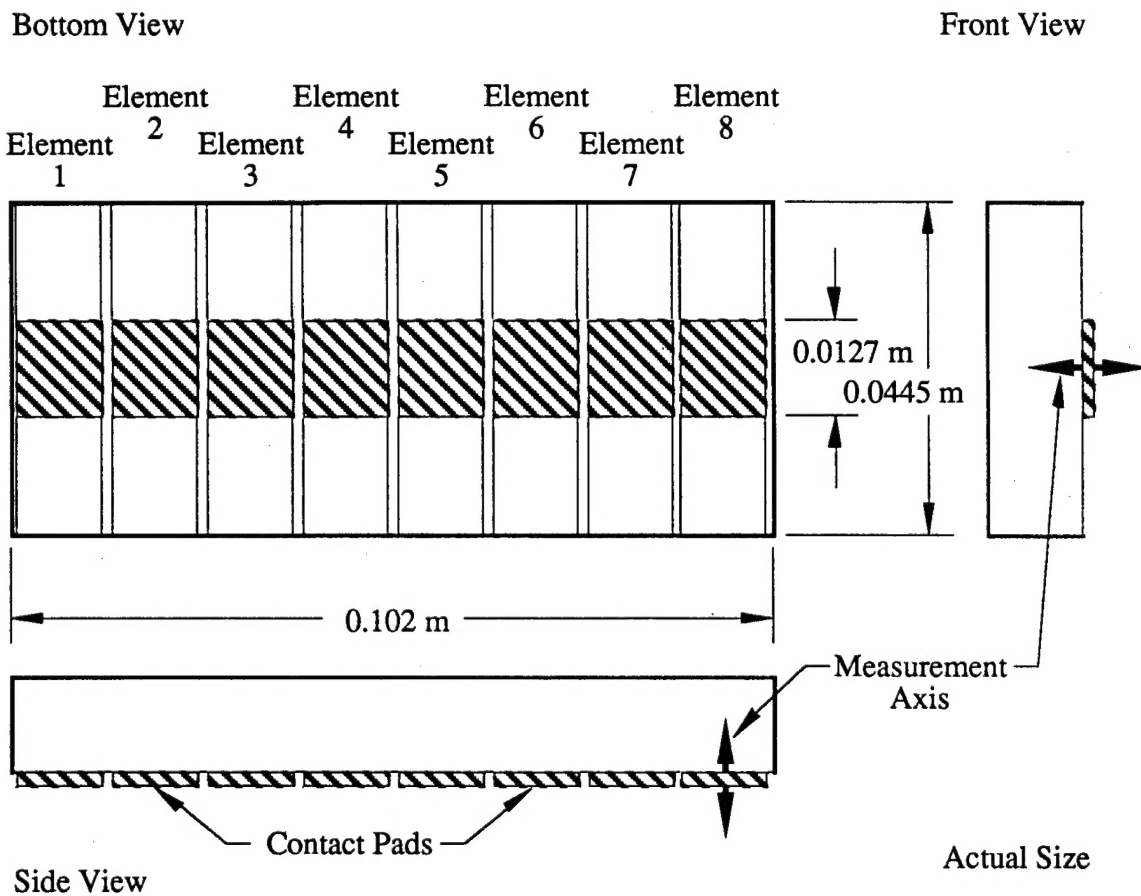
Figure 3. The Eight-Element Array

2. SYSTEM MODEL AND CLOSED-FORM SOLUTION

The system model of the dynamic displacement at the beamformer level is

$$\hat{\Phi}(k_s,\omega_0) = \int_{-\infty}^{\infty} |H(k-k_s)|^2 \, |G(k)|^2 \, |T(k,\omega_0)|^2 \, |P_{tbl}(k,\omega_0)|^2 \, dk \, , \tag{1}$$

where $\hat{\Phi}(k_s,\omega_0)$ is the beamformed displacement wavenumber-frequency spectrum corresponding to the measured output at steered wavenumber k_s (rad/m) and fixed frequency ω_0 (rad/s), $H(k-k_s)$ is the steered response pattern of the array, $G(k)$ is the response pattern of each individual sensor in the array, $T(k,\omega_0)$ is the transfer function between the displacement of the solid at the surface and the normal pressure of the turbulent boundary layer of the fluid acting on the embedded cylindrical shell, $P_{tbl}(k,\omega_0)$ is the streamwise turbulent boundary layer pressure in the fluid, and k is the wavenumber (rad/m). Each of these terms is developed below.

2.1. THE STEERED ARRAY RESPONSE

The normalized wavenumber response of a linear array of N discrete sensors can be modeled as

$$H(k-k_s) = \frac{\sum_{n=1}^{N} w_n e^{i(k-k_s)x_n}}{\sum_{n=1}^{N} w_n} \, , \tag{2a}$$

where x_n is the position of the center of sensor n, and w_n is a spatial weighting function (e.g., Taylor or Hanning). For this analysis, w_n is unity (Boxcar window). For a linearly spaced array, the wavenumber response with uniform shading is

$$H(k-k_s) = \frac{\sin\left[\dfrac{Nd}{2}(k-k_s)\right]}{N\sin\left[\dfrac{d}{2}(k-k_s)\right]} \, , \tag{2b}$$

where d is the center-to-center separation distance of adjacent sensors (m). Equations (2a) and (2b) assume that the sensors are responding as point sensors. Figure 4 is a plot of equation (2b) versus wavenumber. The sensor separation distance (d) is 0.0127 m (0.5 in.) and the number of sensors in the array (N) is eight. The main beam of the array has been steered (k_s) to 150 rad/m. The dashed line corresponds to the unaliased region of the array, which is equal to $\pm \pi / d$ or ± 247.4 rad/m.
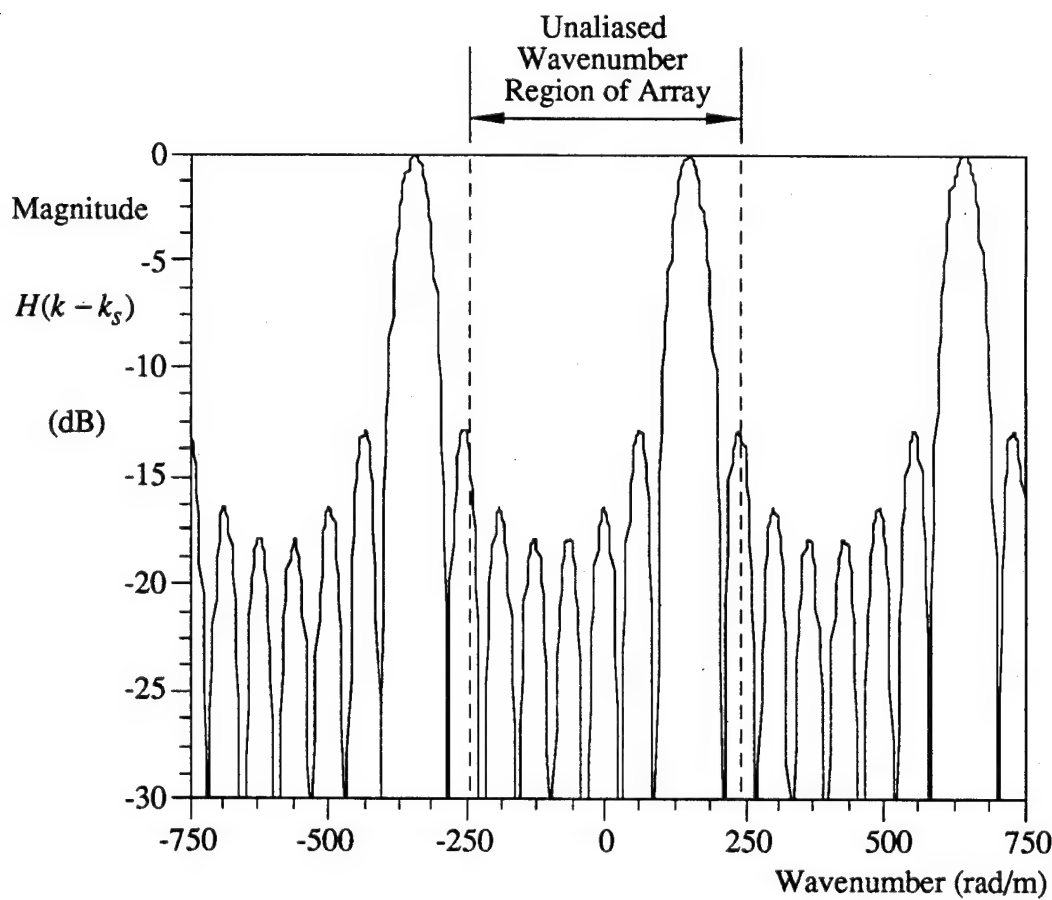
Figure 4. The Theoretical Beam Response of an Eight-Element Array Steered to a Wavenumber of 150 rad/m

2.2. THE INDIVIDUAL SENSOR RESPONSE

The response of each individual sensor is modeled as

$$G(k) = \frac{\sin\left(\dfrac{kL}{2}\right)}{\left(\dfrac{kL}{2}\right)} \quad , \tag{3}$$

where L is the length of the sensor (m). Figure 5 is a plot of equation (3) versus wavenumber. The sensor length (L) is 0.0127 m (0.5 in.). The dashed line corresponds to the unaliased wavenumber region of the array described in section 2.1.
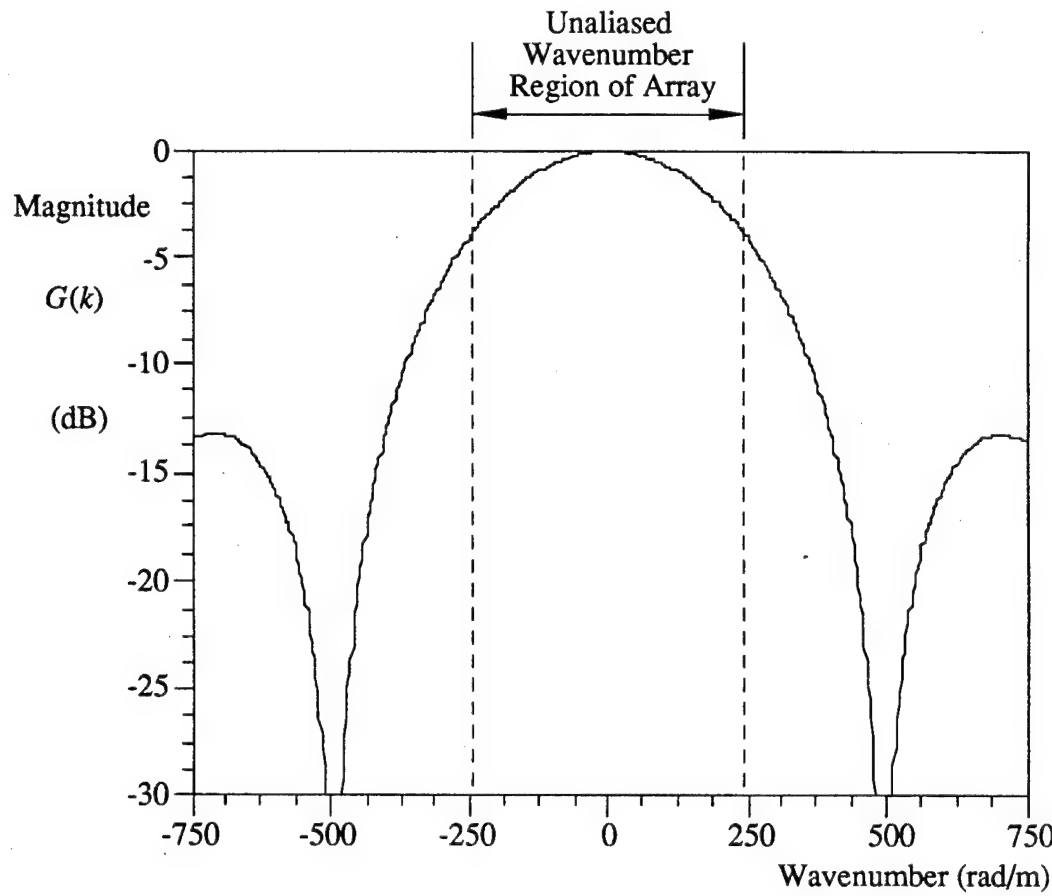
Figure 5. The Theoretical Response of a Sensor That Is 0.0127 m Long

2.3. THE TRANSFER FUNCTION

The transfer function between the vertical displacement of the solid at the top surface and the turbulent boundary layer pressure of the internal fluid is derived by assuming that the system is composed of two concentric cylindrical, linear, isotropic mediums, each governed by the equation (Timoshenko and Goodier, 1934)

$$\mu \nabla^2 \mathbf{u} + (\lambda + \mu) \nabla \nabla \bullet \mathbf{u} = \rho \frac{\partial^2 \mathbf{u}}{\partial t^2} , \tag{4}$$

where ρ is the density; λ and μ are the Lamé constants; t is time; $\bullet$ denotes a vector dot product; $\mathbf{u}$ is the cylindrical coordinate displacement vector expressed as

$$\mathbf{u} = \begin{Bmatrix} u_r(r,\theta,z,t) \\ u_\theta(r,\theta,z,t) \\ u_z(r,\theta,z,t) \end{Bmatrix} , \tag{5}$$

with subscript r denoting the radial direction, θ denoting the angular direction, and z denoting the axial direction; ∇ is the gradient vector differential operator written in cylindrical coordinates as (Potter, 1978)

$$\nabla = \frac{\partial}{\partial r} i_r + \frac{1}{r} \frac{\partial}{\partial \theta} i_\theta + \frac{\partial}{\partial z} i_z , \tag{6}$$

with i_r denoting the unit vector in the r-direction, i_θ denoting the unit vector in the θ-direction, and i_z denoting the unit vector in the z-direction; ∇^2 is the three-dimensional Laplace operator operating on vector $\mathbf{u}$ as

$$\nabla^2 \mathbf{u} = \left(\nabla^2 u_r - \frac{u_r}{r^2} - \frac{2}{r^2} \frac{\partial u_\theta}{\partial \theta} \right) i_r + \left(\nabla^2 u_\theta - \frac{u_\theta}{r^2} + \frac{2}{r^2} \frac{\partial u_r}{\partial \theta} \right) i_\theta + \nabla^2 u_z i_z , \tag{7}$$

with ∇^2 operating on scalar u as

$$\nabla^2 u_{r,\theta,z} = \nabla \bullet \nabla u_{r,\theta,z} = \frac{1}{r} \frac{\partial}{\partial r} \left(r \frac{\partial u_{r,\theta,z}}{\partial r} \right) + \frac{1}{r^2} \frac{\partial^2 u_{r,\theta,z}}{\partial \theta^2} + \frac{\partial^2 u_{r,\theta,z}}{\partial z^2} ; \tag{8}$$

and the term $\nabla \bullet \mathbf{u}$ is called the divergence and is equal to

$$\nabla \bullet \mathbf{u} = \frac{\partial u_r}{\partial r} + \frac{1}{r} \frac{\partial u_\theta}{\partial \theta} + \frac{\partial u_z}{\partial z} + \frac{u_r}{r} . \tag{9}$$

The pressure effects of the fluid acting on the interior surface of the inner cylinder are modeled as structural loads later in this section. The modeled geometry and the coordinate system of the cylinders are shown in figure 6. Note that ρ, λ, and μ are the properties of each specific material. When the modeled region is the embedded cylinder $(a \leq r \leq b)$, the material properties of the surgical tube are used. When the modeled region is the solid block $(b \leq r \leq c)$, the material properties of the urethane are used. The flat surface of the block is modeled as a cylinder, which results in this surface being approximated with a curve. The effects of this approximation, which is necessary to obtain a closed form solution of the displacement field on the block, are discussed later.

The displacement vector **u** is written as

$$\mathbf{u} = \nabla\phi + \nabla \times \mathbf{H} , \tag{10}$$

where ϕ is a dilatational scalar potential, $\times$ denotes a vector cross product, and **H** is an equivoluminal vector potential expressed as

$$\mathbf{H} = \begin{Bmatrix} H_r(r,\theta,z,t) \\ H_\theta(r,\theta,z,t) \\ H_z(r,\theta,z,t) \end{Bmatrix} . \tag{11}$$

Expanding equation (10) and breaking the displacement vector into its individual terms yields

$$u_r = \frac{\partial\phi}{\partial r} + \frac{1}{r}\frac{\partial H_z}{\partial\theta} - \frac{\partial H_\theta}{\partial z} , \tag{12}$$

$$u_\theta = \frac{1}{r}\frac{\partial\phi}{\partial\theta} + \frac{\partial H_r}{\partial z} - \frac{\partial H_z}{\partial r} , \tag{13}$$

and

$$u_z = \frac{\partial\phi}{\partial z} + \frac{H_\theta}{r} + \frac{\partial H_\theta}{\partial r} - \frac{1}{r}\frac{\partial H_r}{\partial\theta} . \tag{14}$$
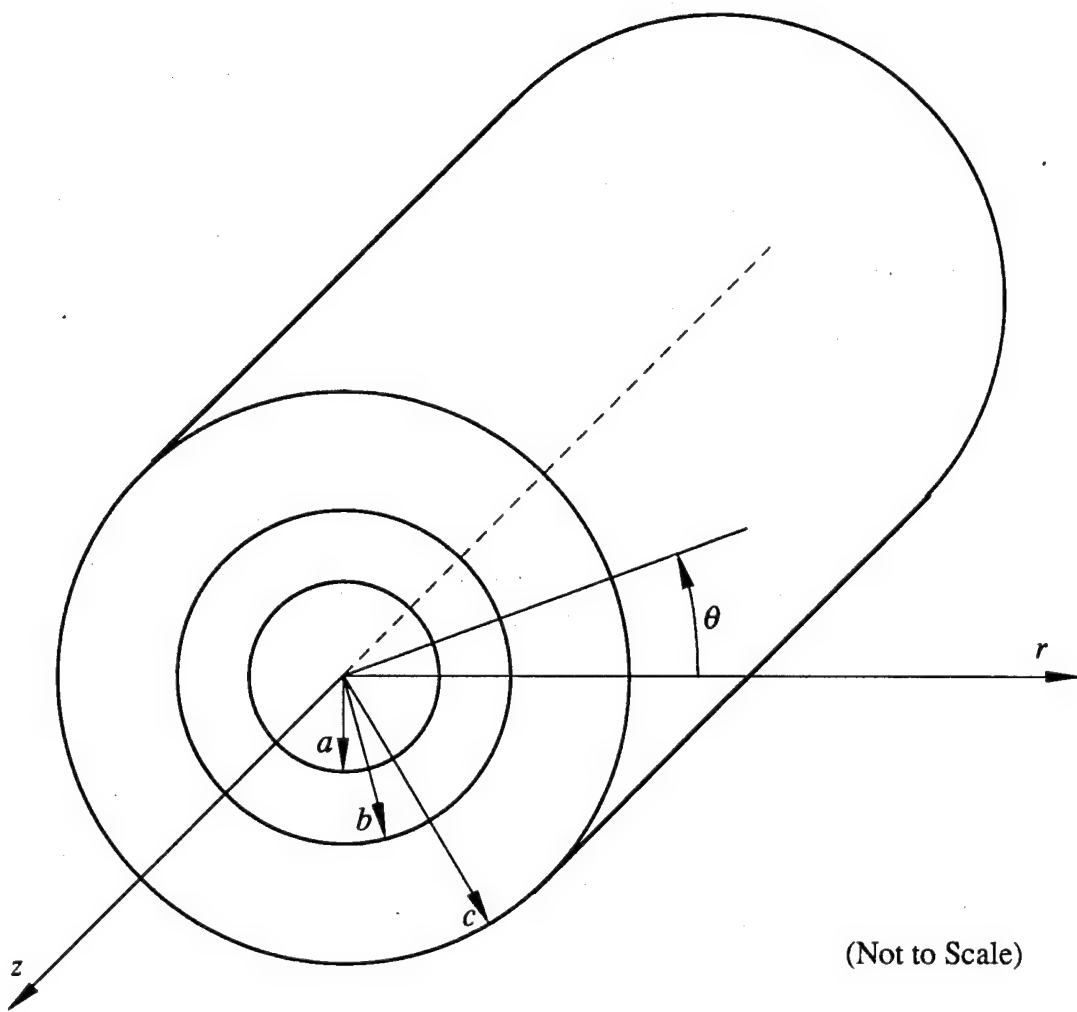
Figure 6. Modeled Geometry With Coordinate System

(Not to Scale)

Equation (10) is next inserted into equation (4), which results in

$$c_d^2 \nabla^2 \phi = \frac{\partial^2 \phi}{\partial t^2}$$ (15)

and

$$c_s^2 \nabla^2 \mathbf{H} = \frac{\partial^2 \mathbf{H}}{\partial t^2}$$ (16)

on both the inner and the outer cylinders. The constants c_d and c_s are the complex dilatational and shear wave speeds, respectively, and are determined by

$$c_d = \sqrt{\frac{\lambda + 2\mu}{\rho}}$$ (17)

and

$$c_s = \sqrt{\frac{\mu}{\rho}} .$$ (18)

The relationship of the Lamé constants to the compressional and shear moduli is shown as

$$\lambda = \frac{E\upsilon}{(1+\upsilon)(1-2\upsilon)}$$ (19)

and

$$\mu = G = \frac{E}{2(1+\upsilon)} ,$$ (20)

where E is the complex compressional modulus (N/m^2), G is the complex shear modulus (N/m^2), and υ is the Poisson's ratio of the material (dimensionless).

The conditions of infinite length, axisymmetric response ($n = 0$), and steady-state response are now imposed, allowing the scalar and vector potential to be written as

$$\phi = g(r)\cos(n\theta)e^{ikz}e^{i\omega t} = g(r)e^{ikz}e^{i\omega t} ,$$ (21)

$$H_r = h_r(r)\sin(n\theta)e^{ikz}e^{i\omega t} \equiv 0 ,$$ (22)

$$H_\theta = h_\theta(r)\cos(n\theta)e^{ikz}e^{i\omega t} = h_\theta(r)e^{ikz}e^{i\omega t} ,$$ (23)

12

and

$$H_z = h_z(r)\sin(n\theta)e^{ikz}e^{i\omega t} \equiv 0 \ , \tag{24}$$

where k is the wavenumber of excitation, ω is the frequency of excitation, and i is the square root of -1. Note that equations (21)-(24) are valid on both the inner and the outer cylinders. For axisymmetric response, the equations of motion are dependent only on the scalar potential ϕ and angular contribution H_θ of the vector potential. Additionally, because $H_r = 0$, $H_z = 0$, and H_θ and ϕ are not functions of θ, equation (13) becomes

$$u_\theta = \frac{\partial(\ )}{\partial\theta} = 0 \ , \tag{25}$$

where ( ) denotes any function. Inserting equations (21)-(24) into equations (15) and (16) yields the following four distinct wave equations on both the inner cylinder and the outer cylinder:

$$\frac{d^2g(r)}{dr^2} + \frac{1}{r}\frac{dg(r)}{dr} + \left(\frac{\omega^2}{c_d^2} - k^2\right)g(r) = 0 \ , \tag{26}$$

$$\frac{d^2h_r(r)}{dr^2} + \frac{1}{r}\frac{dh_r(r)}{dr} + \left(\frac{\omega^2}{c_s^2} - k^2 - \frac{1}{r^2}\right)h_r(r) = 0 \ , \tag{27}$$

$$\frac{d^2h_\theta(r)}{dr^2} + \frac{1}{r}\frac{dh_\theta(r)}{dr} + \left(\frac{\omega^2}{c_s^2} - k^2 - \frac{1}{r^2}\right)h_\theta(r) = 0 \ , \tag{28}$$

and

$$\frac{d^2h_z(r)}{dr^2} + \frac{1}{r}\frac{dh_z(r)}{dr} + \left(\frac{\omega^2}{c_s^2} - k^2\right)h_z(r) = 0 \ . \tag{29}$$

The solutions to equations (26) and (28) are now found on both cylindrical domains with Bessel functions. No solution is found to equations (27) and (29) because they do not contribute to the axisymmetric response. The solution to equation (26) is

$$g(r) = \begin{cases} C_1 J_0(\alpha_1 r) + C_2 Y_0(\alpha_1 r) & a \le r \le b \\ \\ C_5 J_0(\alpha_2 r) + C_6 Y_0(\alpha_2 r) & b \le r \le c \end{cases} , \qquad (30)$$

where J_0 is a complex, zero-order, first-kind standard Bessel function; Y_0 is a complex, zero-order, second-kind standard Bessel function; C_1, C_2, C_5, and C_6 are complex constants (determined below); α_1 is defined on the inner cylinder as

$$\alpha_1 = \sqrt{\frac{\omega^2}{c_{d1}^2} - k^2} , \qquad (31)$$

where the subscript $d1$ refers to the complex dilatational wave speed in the inner cylinder; and α_2 is defined on the outer cylinder as

$$\alpha_2 = \sqrt{\frac{\omega^2}{c_{d2}^2} - k^2} , \qquad (32)$$

where the subscript $d2$ refers to the complex dilatational wave speed in the outer cylinder. The solution to equation (28) is

$$h_\theta(r) = \begin{cases} C_3 J_1(\beta_1 r) + C_4 Y_1(\beta_1 r) & a \le r \le b \\ \\ C_7 J_1(\beta_2 r) + C_8 Y_1(\beta_2 r) & b \le r \le c \end{cases} , \qquad (33)$$

where J_1 is a complex, first-order, first-kind standard Bessel function; Y_1 is a complex, first-order, second-kind standard Bessel function; C_3, C_4, C_7, and C_8 are complex constants (determined below); β_1 is defined on the inner cylinder as

$$\beta_1 = \sqrt{\frac{\omega^2}{c_{s1}^2} - k^2} , \qquad (34)$$

where the subscript $s1$ refers to the complex shear wave speed in the inner cylinder; and β_2 is defined on the outer cylinder as

$$\beta_2 = \sqrt{\frac{\omega^2}{c_{s2}^2} - k^2} , \qquad (35)$$

14

where the subscript $s2$ refers to the complex shear wave speed in the outer cylinder.

The strains are related to the displacements in an axisymmetric solid by (Timoshenko and Goodier, 1934)

$$\varepsilon_{rr} = \frac{\partial u_r}{\partial r} , \tag{36}$$

$$\varepsilon_{\theta\theta} = \frac{u_r}{r} , \tag{37}$$

$$\varepsilon_{zz} = \frac{\partial u_z}{\partial z} , \tag{38}$$

and

$$\varepsilon_{rz} = \frac{1}{2}\left(\frac{\partial u_z}{\partial r} + \frac{\partial u_r}{\partial z}\right) . \tag{39}$$

The relationship between the displacements (and the derivatives of the displacements) and the potential functions g and h_θ is found by combining equations (12), (14), (21), and (23) to produce

$$u_r = \left(\frac{dg(r)}{dr} - ikh_\theta(r)\right)e^{ikz}e^{i\omega t} , \tag{40}$$

$$u_z = \left(ikg(r) + \frac{h_\theta(r)}{r} + \frac{dh_\theta(r)}{dr}\right)e^{ikz}e^{i\omega t} , \tag{41}$$

$$\frac{\partial u_r}{\partial r} = \left(\frac{d^2 g(r)}{dr^2} - ik\frac{dh_\theta(r)}{dr}\right)e^{ikz}e^{i\omega t} , \tag{42}$$

$$\frac{\partial u_z}{\partial z} = \left(-k^2 g(r) + \frac{ikh_\theta(r)}{r} + ik\frac{dh_\theta(r)}{dr}\right)e^{ikz}e^{i\omega t} , \tag{43}$$

$$\frac{\partial u_z}{\partial r} = \left(ik\frac{dg(r)}{dr} + \frac{1}{r}\frac{dh_\theta(r)}{dr} - \frac{h_\theta(r)}{r^2} + \frac{d^2 h_\theta(r)}{dr^2}\right)e^{ikz}e^{i\omega t} , \tag{44}$$

and

$$\frac{\partial u_r}{\partial z} = \left(ik\frac{dg(r)}{dr} + k^2 h_\theta(r)\right)e^{ikz}e^{i\omega t} . \tag{45}$$

The displacements and external forces are now equated by use of the stress-strain constitutive equations on the free surfaces of the cylinders and at the inner and outer cylinder interface. The normal stress, strain, and radial forces acting on the inner cylinder at radius a are related by

$$\sigma_{rr}(a,z,t) = (\lambda_1 + 2\mu_1)\varepsilon_{rr}(a,z,t) + \lambda_1\varepsilon_{\theta\theta}(a,z,t) + \lambda_1\varepsilon_{zz}(a,z,t) = p_i(a,z,t) \quad, \quad (46)$$

where $\sigma_{rr}(a,z,t)$ is the normal radial stress, $\varepsilon_{rr}(a,z,t)$ is the normal radial strain, $\varepsilon_{\theta\theta}(a,z,t)$ is the normal circumferential strain, $\varepsilon_{zz}(a,z,t)$ is the normal longitudinal strain, $p_i(a,z,t)$ is the internal pressure acting on the cylinder in the radial direction, and the subscript 1 denotes material properties of the inner cylinder. The shear stress, strain, and longitudinal forces acting on the inner cylinder at radius a are related by

$$\sigma_{rz}(a,z,t) = 2\mu_1\varepsilon_{rz}(a,z,t) = f_i(a,z,t) \quad, \quad (47)$$

where $\sigma_{rz}(a,z,t)$ is the shear stress, $\varepsilon_{rz}(a,z,t)$ is the shear strain, and $f_i(a,z,t)$ is the internal shear stress acting on the inner cylinder in the longitudinal direction. At the interface of the cylinders, the displacements and stresses of the inner cylinder are matched to the displacements and stresses of the outer cylinder. These boundary interface equations are written as

$$u_r(b_-,z,t) = u_r(b_+,z,t) \quad, \quad (48)$$

$$u_z(b_-,z,t) = u_z(b_+,z,t) \quad, \quad (49)$$

$$\sigma_{rr}(b_-,z,t) = \sigma_{rr}(b_+,z,t) \quad, \quad (50)$$

and

$$\sigma_{rz}(b_-,z,t) = \sigma_{rz}(b_+,z,t) \quad, \quad (51)$$

where the minus subscript corresponds to equations evaluated using the inner cylinder properties and the plus subscript corresponds to equations evaluated using the outer cylinder properties. The normal stress, strain, and radial forces acting on the outer cylinder at radius c are related by

$$\sigma_{rr}(c,z,t) = (\lambda_2 + 2\mu_2)\varepsilon_{rr}(c,z,t) + \lambda_2\varepsilon_{\theta\theta}(c,z,t) + \lambda_2\varepsilon_{zz}(c,z,t) = p_o(c,z,t) \quad, \quad (52)$$

16

where $p_o(c,z,t)$ is the external pressure acting on the cylinder in the radial direction, and the subscript 2 denotes material properties of the outer cylinder. The shear stress, strain, and longitudinal forces acting on the outer cylinder at radius c are related by

$$\sigma_{rz}(c,z,t) = 2\mu_2\varepsilon_{rz}(c,z,t) = f_o(c,z,t) \quad, \tag{53}$$

where $\sigma_{rz}(c,z,t)$ is the shear stress, $\varepsilon_{rz}(c,z,t)$ is the shear strain, and $f_o(c,z,t)$ is the external shear stress acting on the outer cylinder in the longitudinal direction.

Combining equations (36), (37), (38), (40), (42), and (46) yields the normal stress in terms of the potential functions g and h_θ at $r = a$ as

$$(\lambda_1 + 2\mu_1)\frac{d^2g(a)}{dr^2} + \frac{\lambda_1}{a}\frac{dg(a)}{dr} - \lambda_1 k^2 g(a) - 2\mu_1 ik\frac{d^2h_\theta(a)}{dr^2} = P_i \, , \tag{54}$$

where P_i is the magnitude of the normal force acting on the interior of the inner cylinder. Combining equations (39), (44), (45), and (47) yields the shear stress in terms of the potential functions g and h_θ at $r = a$. The result is

$$2\mu_1 ik\frac{dg(a)}{dr} + \left(\mu_1 k^2 - \frac{\mu_1}{a^2}\right)h_\theta(a) + \frac{\mu_1}{a}\frac{dh_\theta(a)}{dr} + \mu_1\frac{d^2h_\theta(a)}{dr^2} = F_i \, , \tag{55}$$

where F_i is the magnitude of the externally applied shear stress acting on the interior of the inner cylinder. Equations (40) and (48) are combined to yield the radial displacement interface equation

$$\frac{dg(b_-)}{dr} - ikh_\theta(b_-) = \frac{dg(b_+)}{dr} - ikh_\theta(b_+) \, , \tag{56}$$

and equations (41) and (49) are combined to produce the longitudinal displacement interface equation

$$ikg(b_-) + \frac{h_\theta(b_-)}{r} + \frac{dh_\theta(b_-)}{dr} = ikg(b_+) + \frac{h_\theta(b_+)}{r} + \frac{dh_\theta(b_+)}{dr} \, . \tag{57}$$

Equations (36), (37), (38), (40), (42), and (50) are combined to yield the normal radial stress interface equation

$$(\lambda_1 + 2\mu_1)\frac{d^2g(b_-)}{dr^2} + \frac{\lambda_1}{b}\frac{dg(b_-)}{dr} - \lambda_1 k^2 g(b_-) - 2\mu_1 ik\frac{d^2h_\theta(b_-)}{dr^2} =$$

$$(\lambda_2 + 2\mu_2)\frac{d^2g(b_+)}{dr^2} + \frac{\lambda_2}{b}\frac{dg(b_+)}{dr} - \lambda_2 k^2 g(b_+) - 2\mu_2 ik\frac{d^2h_\theta(b_+)}{dr^2} , \qquad (58)$$

and equations (39), (44), (45), and (51) are combined to produce the shear stress interface equation

$$2\mu_1 ik\frac{dg(b_-)}{dr} + \left(\mu_1 k^2 - \frac{\mu_1}{b^2}\right)h_\theta(b_-) + \frac{\mu_1}{b}\frac{dh_\theta(b_-)}{dr} + \mu_1\frac{d^2h_\theta(b_-)}{dr^2} =$$

$$2\mu_2 ik\frac{dg(b_+)}{dr} + \left(\mu_2 k^2 - \frac{\mu_2}{b^2}\right)h_\theta(b_+) + \frac{\mu_2}{b}\frac{dh_\theta(b_+)}{dr} + \mu_2\frac{d^2h_\theta(b_+)}{dr^2} . \qquad (59)$$

Combining equations (36), (37), (38), (40), (42), and (52) yields the normal stress in terms of the potential functions g and h_θ at $r = c$ as

$$(\lambda_2 + 2\mu_2)\frac{d^2g(c)}{dr^2} + \frac{\lambda_2}{c}\frac{dg(c)}{dr} - \lambda_2 k^2 g(c) - 2\mu_2 ik\frac{d^2h_\theta(c)}{dr^2} = P_o , \qquad (60)$$

where P_o is the magnitude of the normal force acting on the exterior of the outer cylinder. Combining equations (39), (44), (45), and (53) yields the shear stress in terms of the potential functions g and h_θ at $r = c$. The result is

$$2\mu_2 ik\frac{dg(c)}{dr} + \left(\mu_2 k^2 - \frac{\mu_2}{c^2}\right)h_\theta(c) + \frac{\mu_2}{c}\frac{dh_\theta(c)}{dr} + \mu_2\frac{d^2h_\theta(c)}{dr^2} = F_o , \qquad (61)$$

where F_o is the magnitude of the externally applied shear stress acting on the exterior of the outer cylinder. Implicit in equations (54)-(61) is the assumption that the external loads on the cylinder are occurring at a definite frequency and wavenumber.

Inserting equations (30) and (33) into equations (54)-(61), applying the recurrence relationships of the first- and second-kind standard Bessel functions, and then rewriting as an eight-by-eight system of linear equations results in

$$\begin{bmatrix} a_{11} & a_{12} & a_{13} & a_{14} & a_{15} & a_{16} & a_{17} & a_{18} \\ a_{21} & a_{22} & a_{23} & a_{24} & a_{25} & a_{26} & a_{27} & a_{28} \\ a_{31} & a_{32} & a_{33} & a_{34} & a_{35} & a_{36} & a_{37} & a_{38} \\ a_{41} & a_{42} & a_{43} & a_{44} & a_{45} & a_{46} & a_{47} & a_{48} \\ a_{51} & a_{52} & a_{53} & a_{54} & a_{55} & a_{56} & a_{57} & a_{58} \\ a_{61} & a_{62} & a_{63} & a_{64} & a_{65} & a_{66} & a_{67} & a_{68} \\ a_{71} & a_{72} & a_{73} & a_{74} & a_{75} & a_{76} & a_{77} & a_{78} \\ a_{81} & a_{82} & a_{83} & a_{84} & a_{85} & a_{86} & a_{87} & a_{88} \end{bmatrix} \begin{Bmatrix} C_1 \\ C_2 \\ C_3 \\ C_4 \\ C_5 \\ C_6 \\ C_7 \\ C_8 \end{Bmatrix} = \begin{Bmatrix} P_i \\ F_i \\ 0 \\ 0 \\ 0 \\ 0 \\ P_o \\ F_o \end{Bmatrix} , \tag{62}$$

where the matrix coefficients a_{nm} are given as

$$a_{11} = \left[(-\lambda_1 - 2\mu_1)\alpha_1^2 - \lambda_1 k^2\right] J_0(\alpha_1 a) + \left(\frac{2\mu_1\alpha_1}{a}\right) J_1(\alpha_1 a) , \tag{63}$$

$$a_{12} = \left[(-\lambda_1 - 2\mu_1)\alpha_1^2 - \lambda_1 k^2\right] Y_0(\alpha_1 a) + \left(\frac{2\mu_1\alpha_1}{a}\right) Y_1(\alpha_1 a) , \tag{64}$$

$$a_{13} = (-2\mu_1 ik\beta_1) J_0(\beta_1 a) + \left(\frac{2\mu_1 ik}{a}\right) J_1(\beta_1 a) , \tag{65}$$

$$a_{14} = (-2\mu_1 ik\beta_1) Y_0(\beta_1 a) + \left(\frac{2\mu_1 ik}{a}\right) Y_1(\beta_1 a) , \tag{66}$$

$$a_{15} = 0 , \tag{67}$$

$$a_{16} = 0 , \tag{68}$$

$$a_{17} = 0 , \tag{69}$$

$$a_{18} = 0 , \tag{70}$$

$$a_{21} = (-2\mu_1 ik\alpha_1) J_1(\alpha_1 a) , \tag{71}$$

$$a_{22} = (-2\mu_1 ik\alpha_1) Y_1(\alpha_1 a) , \tag{72}$$

$$a_{23} = [\mu_1(k^2 - \beta_1^2)] J_1(\beta_1 a) , \tag{73}$$

$$a_{24} = [\mu_1(k^2 - \beta_1^2)] Y_1(\beta_1 a) , \tag{74}$$

$$a_{25} = 0 , \tag{75}$$

19

$$a_{26} = 0 \ , \tag{76}$$

$$a_{27} = 0 \ , \tag{77}$$

$$a_{28} = 0 \ , \tag{78}$$

$$a_{31} = -\alpha_1 J_1(\alpha_1 b) \ , \tag{79}$$

$$a_{32} = -\alpha_1 Y_1(\alpha_1 b) \ , \tag{80}$$

$$a_{33} = -ik J_1(\beta_1 b) \ , \tag{81}$$

$$a_{34} = -ik Y_1(\beta_1 b) \ , \tag{82}$$

$$a_{35} = \alpha_2 J_1(\alpha_2 b) \ , \tag{83}$$

$$a_{36} = \alpha_2 Y_1(\alpha_2 b) \ , \tag{84}$$

$$a_{37} = ik J_1(\beta_2 b) \ , \tag{85}$$

$$a_{38} = ik Y_1(\beta_2 b) \ , \tag{86}$$

$$a_{41} = ik J_0(\alpha_1 b) \ , \tag{87}$$

$$a_{42} = ik Y_0(\alpha_1 b) \ , \tag{88}$$

$$a_{43} = \beta_1 J_0(\beta_1 b) \ , \tag{89}$$

$$a_{44} = \beta_1 Y_0(\beta_1 b) \ , \tag{90}$$

$$a_{45} = -ik J_0(\alpha_2 b) \ , \tag{91}$$

$$a_{46} = -ik Y_0(\alpha_2 b) \ , \tag{92}$$

$$a_{47} = -\beta_2 J_0(\beta_2 b) \ , \tag{93}$$

$$a_{48} = -\beta_2 Y_0(\beta_2 b) \ , \tag{94}$$

$$a_{51} = \left[(-\lambda_1 - 2\mu_1)\alpha_1^2 - \lambda_1 k^2 \right] J_0(\alpha_1 b) + \left(\frac{2\mu_1\alpha_1}{b} \right) J_1(\alpha_1 b) \ , \tag{95}$$

$$a_{52} = \left[(-\lambda_1 - 2\mu_1)\alpha_1^2 - \lambda_1 k^2 \right] Y_0(\alpha_1 b) + \left(\frac{2\mu_1\alpha_1}{b} \right) Y_1(\alpha_1 b) \ , \tag{96}$$

$$a_{53} = (-2\mu_1 ik\beta_1)J_0(\beta_1 b) + \left(\frac{2\mu_1 ik}{b}\right)J_1(\beta_1 b) \ , \tag{97}$$

$$a_{54} = (-2\mu_1 ik\beta_1)Y_0(\beta_1 b) + \left(\frac{2\mu_1 ik}{b}\right)Y_1(\beta_1 b) \ , \tag{98}$$

$$a_{55} = \left[(\lambda_2 + 2\mu_2)\alpha_2^2 + \lambda_2 k^2\right]J_0(\alpha_2 b) - \left(\frac{2\mu_2 \alpha_2}{b}\right)J_1(\alpha_2 b) \ , \tag{99}$$

$$a_{56} = \left[(\lambda_2 + 2\mu_2)\alpha_2^2 + \lambda_2 k^2\right]Y_0(\alpha_2 b) - \left(\frac{2\mu_2 \alpha_2}{b}\right)Y_1(\alpha_2 b) \ , \tag{100}$$

$$a_{57} = (2\mu_2 ik\beta_2)J_0(\beta_2 b) - \left(\frac{2\mu_2 ik}{b}\right)J_1(\beta_2 b) \ , \tag{101}$$

$$a_{58} = (2\mu_2 ik\beta_2)Y_0(\beta_2 b) - \left(\frac{2\mu_2 ik}{b}\right)Y_1(\beta_2 b) \ , \tag{102}$$

$$a_{61} = (-2\mu_1 ik\alpha_1)J_1(\alpha_1 b) \ , \tag{103}$$

$$a_{62} = (-2\mu_1 ik\alpha_1)Y_1(\alpha_1 b) \ , \tag{104}$$

$$a_{63} = [\mu_1(k^2 - \beta_1^2)]J_1(\beta_1 b) \ , \tag{105}$$

$$a_{64} = [\mu_1(k^2 - \beta_1^2)]Y_1(\beta_1 b) \ , \tag{106}$$

$$a_{65} = (2\mu_2 ik\alpha_2)J_1(\alpha_2 b) \ , \tag{107}$$

$$a_{66} = (2\mu_2 ik\alpha_2)Y_1(\alpha_2 b) \ , \tag{108}$$

$$a_{67} = [-\mu_2(k^2 - \beta_2^2)]J_1(\beta_2 b) \ , \tag{109}$$

$$a_{68} = [-\mu_2(k^2 - \beta_2^2)]Y_1(\beta_2 b) \ , \tag{110}$$

$$a_{71} = 0 \ , \tag{111}$$

$$a_{72} = 0 \ , \tag{112}$$

$$a_{73} = 0 \ , \tag{113}$$

$$a_{74} = 0 \ , \tag{114}$$

$$a_{75} = \left[(-\lambda_2 - 2\mu_2)\alpha_2^2 - \lambda_2 k^2\right]J_0(\alpha_2 c) + \left(\frac{2\mu_2 \alpha_2}{c}\right)J_1(\alpha_2 c) \ , \tag{115}$$

21

$$a_{76} = \left[(-\lambda_2 - 2\mu_2)\alpha_2^2 - \lambda_2 k^2 \right] Y_0(\alpha_2 c) + \left(\frac{2\mu_2 \alpha_2}{c} \right) Y_1(\alpha_2 c) \ , \tag{116}$$

$$a_{77} = (-2\mu_2 i k \beta_2) J_0(\beta_2 c) + \left(\frac{2\mu_2 i k}{c} \right) J_1(\beta_2 c) \ , \tag{117}$$

$$a_{78} = (-2\mu_2 i k \beta_2) Y_0(\beta_2 c) + \left(\frac{2\mu_2 i k}{c} \right) Y_1(\beta_2 c) \ , \tag{118}$$

$$a_{81} = 0 \ , \tag{119}$$

$$a_{82} = 0 \ , \tag{120}$$

$$a_{83} = 0 \ , \tag{121}$$

$$a_{84} = 0 \ , \tag{122}$$

$$a_{85} = (-2\mu_2 i k \alpha_2) J_1(\alpha_2 c) \ , \tag{123}$$

$$a_{86} = (-2\mu_2 i k \alpha_2) Y_1(\alpha_2 c) \ , \tag{124}$$

$$a_{87} = [\mu_2(k^2 - \beta_2^2)] J_1(\beta_2 c) \ , \tag{125}$$

and

$$a_{88} = [\mu_2(k^2 - \beta_2^2)] Y_1(\beta_2 c) \ . \tag{126}$$

The interior pressure field p_i at the inner cylinder a is now broken into two components: one models the normal wall pressure in the turbulent boundary layer and the other models the acoustic pressure in the fluid. This interior pressure term is written as

$$p_i(a,z,t) = p_{tbl}(a,z,t) - p(a,z,t) \ , \tag{127}$$

where the subscript tbl denotes the term associated with the turbulent boundary layer and is discussed in the next section. The acoustic pressure in the fluid is derived from the wave equation written in cylindrical coordinates as

$$\frac{\partial^2 p(r,z,t)}{\partial t^2} = c_f^2 \left[\frac{\partial^2 p(r,z,t)}{\partial r^2} + \frac{1}{r} \frac{\partial p(r,z,t)}{\partial r} + \frac{\partial^2 p(r,z,t)}{\partial z^2} \right] \ , \tag{128}$$

22

where c_f is the compressional wave speed in the fluid (m/s). The assumption is made in equation (128) that Mach number effects on the wave equation are negligible because the fluid is flowing at a sufficiently slow speed. The boundary condition on the fluid/structure interface is written, using conservation of linear momentum, as

$$\frac{\partial p(a,z,t)}{\partial r} = -\rho_f \frac{\partial^2 u_r(a,z,t)}{\partial t^2} \; . \tag{129}$$

The acoustic pressure field is modeled as a magnitude with definite frequency and wavenumber content as

$$p(r,z,t) = P(r)e^{ikz}e^{i\omega t} \; . \tag{130}$$

Inserting equation (130) into equation (128) yields

$$\frac{d^2 P(r)}{dr^2} + \frac{1}{r}\frac{dP(r)}{dr} + \left(\frac{\omega^2}{c_f^2} - k^2\right)P(r) = 0 \; . \tag{131}$$

The solution to equation (131) is

$$P(r) = C_9 J_0(\gamma r) \; , \tag{132}$$

where C_9 is a constant (shown implicitly in equation (135)) and

$$\gamma = \sqrt{\frac{\omega^2}{c_f^2} - k^2} \; . \tag{133}$$

It is implicit in the solution to equation (131) that the pressure in the interior fluid is finite. Writing the radial displacement as

$$u_r(r,z,t) = U_r(r)e^{ikz}e^{i\omega t} \tag{134}$$

and then inserting equation (132) into the boundary condition (equation (129)) yields

$$P(a) = \frac{-\rho_f \omega^2 J_0(\gamma a)}{\gamma J_1(\gamma a)}U_r(a) \; . \tag{135}$$

It is now noted, based on equations (12), (30), (33), (40), and (134), that

$$U_r(a) = -C_1\alpha_1 J_1(\alpha_1 a) - C_2\alpha_1 Y_1(\alpha_1 a) - C_3 ik J_1(\beta_1 a) - C_4 ik Y_1(\beta_1 a) \; . \tag{136}$$

Combining equations (135) and (136) yields

$$P(a) = C_1 \frac{\rho_f \omega^2 J_0(\gamma a)\alpha_1 J_1(\alpha_1 a)}{\gamma J_1(\gamma a)} + C_2 \frac{\rho_f \omega^2 J_0(\gamma a)\alpha_1 Y_1(\alpha_1 a)}{\gamma J_1(\gamma a)}$$

$$+ C_3 \frac{\rho_f \omega^2 J_0(\gamma a)ik J_1(\beta_1 a)}{\gamma J_1(\gamma a)} + C_4 \frac{\rho_f \omega^2 J_0(\gamma a)ik Y_1(\beta_1 a)}{\gamma J_1(\gamma a)} \ . \tag{137}$$

Equation (137) is inserted into equation (62), which results in the **A** matrix coefficients a_{11}, a_{12}, a_{13}, and a_{14} being modified to

$$a_{11} = \left[(-\lambda_1 - 2\mu_1)\alpha_1^2 - \lambda_1 k^2\right]J_0(\alpha_1 a) + \left(\frac{2\mu_1\alpha_1}{a} + \frac{\rho_f \omega^2 J_0(\gamma a)\alpha_1}{\gamma J_1(\gamma a)}\right)J_1(\alpha_1 a) \ , \tag{138}$$

$$a_{12} = \left[(-\lambda_1 - 2\mu_1)\alpha_1^2 - \lambda_1 k^2\right]Y_0(\alpha_1 a) + \left(\frac{2\mu_1\alpha_1}{a} + \frac{\rho_f \omega^2 J_0(\gamma a)\alpha_1}{\gamma J_1(\gamma a)}\right)Y_1(\alpha_1 a) \ , \tag{139}$$

$$a_{13} = (-2\mu_1 ik\beta_1)J_0(\beta_1 a) + \left(\frac{2\mu_1 ik}{a} + \frac{\rho_f \omega^2 J_0(\gamma a)ik}{\gamma J_1(\gamma a)}\right)J_1(\beta_1 a) \ , \tag{140}$$

and

$$a_{14} = (-2\mu_1 ik\beta_1)Y_0(\beta_1 a) + \left(\frac{2\mu_1 ik}{a} + \frac{\rho_f \omega^2 J_0(\gamma a)ik}{\gamma J_1(\gamma a)}\right)Y_1(\beta_1 a) \ . \tag{141}$$

The remaining terms in the **A** matrix are unchanged. Additionally, the external shear stresses at a and c and the external normal pressure at c are assumed to be equal to zero, resulting in a load vector of

$$\begin{Bmatrix} P_{tbl} \\ 0 \\ 0 \\ 0 \\ 0 \\ 0 \\ 0 \\ 0 \end{Bmatrix} \ . \tag{142}$$

Now that the **A** matrix and the load vector are known, a solution to the constants C_1 through C_8 can be determined by inverting the **A** matrix and multiplying it by the load vector in equation (142). Once the constants are known, the radial displacement at c divided by the interior turbulent boundary layer pressure can be determined with an expression similar to equation (136):

$$T(k,\omega_0) = \frac{U_r(c)}{P_{tbl}} = -C_5\alpha_2 J_1(\alpha_2 c) - C_6\alpha_2 Y_1(\alpha_2 c) - C_7 i k J_1(\beta_2 c) - C_8 i k Y_1(\beta_2 c) \ . \qquad (143)$$

Figure 7 is a plot of the transfer function of radial displacement divided by the turbulent boundary layer pressure versus wavenumber. The frequency of the transfer function is 250 Hz, the inner radius (a) is 0.00159 m (1/16 in.), the middle radius (b) is 0.00238 m (3/32 in.), and the outer radius (c) is 0.00191 m (3/4 in.). For the inner cylinder, the dilatational (compressional) modulus (E_1) is $(1+0.18i) \times 10^6$ N/m^2, the Poisson's ratio (υ_1) is 0.49 (dimensionless), the shear modulus (G_1) is $3.4(1+0.18i) \times 10^5$ N/m^2, and the density is 1000 kg/m^3. For the outer cylinder, the dilatational modulus (E_2) is $1.9(1+0.30i) \times 10^5$ N/m^2, the Poisson's ratio (υ_2) is 0.49 (dimensionless), the shear modulus (G_2) is $6.4(1+0.30i) \times 10^5$ N/m^2, and the density is 930 kg/m^3. The speed of a compressional wave in the fluid (c_f) is 1500 m/s and the density of the fluid (ρ_f) is 1000 kg/m^3. Note that the dynamic range of the magnitude of the transfer function is approximately 100 dB in the wavenumber range $-750 < k < 750$ rad/m. The relative minima in the transfer function that occurs at ± 64 rad/m correspond to a fluid/structure interaction bulge wave. The maxima of the transfer function correspond to shear wave propagation.
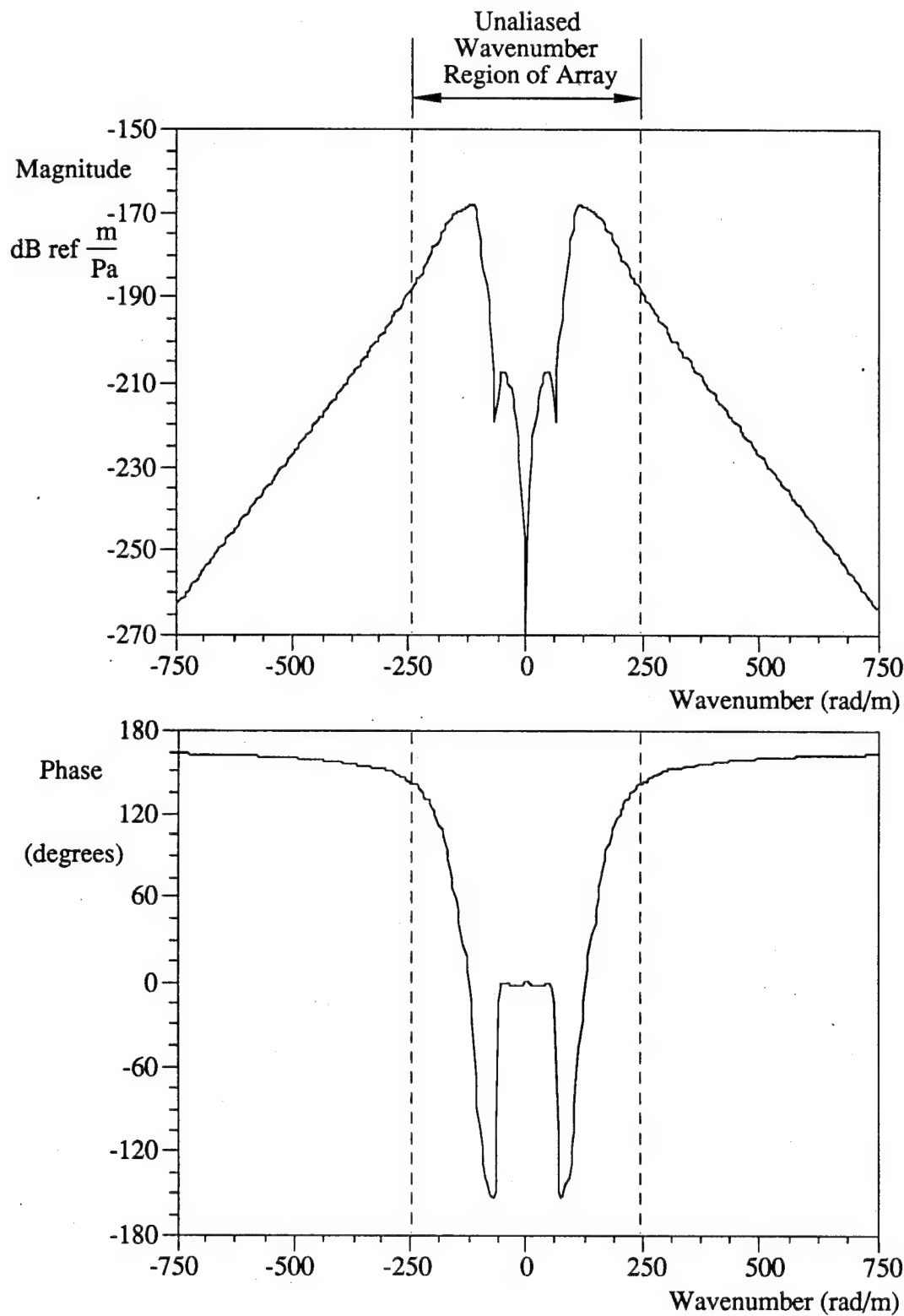
Figure 7. Transfer Function of Radial Displacement Divided by Turbulent Boundary Layer Pressure

2.4. THE SOURCE

The source of energy for the excitation of the viscoelastic material under consideration is from the flow of fluid through the small diameter flexible cylinder. It is assumed that the flow through the pipe is fully developed, turbulent, and incompressible. The pressure at the fluid-solid interface is known as the "wall" pressure. The space-time characteristics of this energy are used as input to the structural response model for the viscoelastic material.

No measurements of the wall pressure for turbulent flow inside a small diameter cylinder are known to exist. Spectral measurements in larger cylinders, however, have been found to agree well with those made on a flat plate (Bakewell et al., 1962). The source model of the normal pressure of the turbulent boundary layer in the cylinder is therefore derived from a previously formulated flat plate wall pressure spectrum model (Chase, 1987). Because it is convenient to work in the spectral, or Fourier-transform, domain, the model represents the two-wavenumber/frequency spectrum of the wall pressure as opposed to the space-time correlation function. The spanwise dimension of the flat plate is replaced by the circumferential dimension of the cylinder in which the fluid flows. This translation is achieved by applying a filter function in the spanwise wavenumber domain to the two-wavenumber/frequency spectrum. The result is the circumferentially averaged or "mode 0" component of the streamwise wavenumber-frequency spectrum of the pressure inside the cylinder.

The model of the two-wavenumber/frequency spectrum of wall pressure for incompressible flow over a flat plate is given as (Chase, 1987)

$$|P(k,k_2,\omega_0)|^2 = \frac{\rho_f^2 \, \upsilon_*^3}{\left[K_+^2 + (b\delta)^{-2}\right]^{5/2}} \left\{ C_T \left(k^2 + k_2^2\right) \left[\frac{K_+^2 + (b\delta)^{-2}}{k^2 + k_2^2 + (b\delta)^{-2}} \right] + C_M k^2 \right\}, \quad (144)$$

where k is the wavenumber of the streamwise component of the flow (rad/m); k_2 is the wavenumber of the spanwise component of the flow (rad/m); υ_* is the friction velocity (m/s); δ is the boundary layer thickness (m); C_T, C_M, and b are constants; and

$$K_+^2 = \frac{(\omega_0 - u_c k)^2}{(h\upsilon_*)^2} + k^2 + k_2^2 \,, \quad (145)$$

27

where u_c is the convection velocity (m/s) and h is a constant. A positive value of k corresponds to fluid energy moving downstream. The convection velocity is assumed to be equal to the mean flow velocity, $\bar{u}$, and they will be used interchangeably in the following derivations. The friction velocity by definition is

$$v_* = \sqrt{\frac{\tau_w}{\rho_f}} \ , \tag{146}$$

where τ_w is the shear stress at the wall (N/m^2). The mean wall shear stress inside a cylinder is approximated by

$$\tau_w = \frac{\rho_f \bar{u}^2 f}{8} \ , \tag{147}$$

where f is the friction factor. For smooth pipes, the friction factor is (Fox and McDonald, 1985)

$$f = \frac{0.3164}{(\text{Re}_d)^{0.25}} \ , \tag{148}$$

where Re_d is the Reynolds number of the flow calculated using the maximum (centerline) pipe velocity. The ratio of the centerline velocity to the mean flow is (Fox and McDonald, 1985)

$$\frac{\bar{u}}{U} = \frac{2n^2}{(n+1)(2n+1)} \ , \tag{149}$$

where U is the centerline velocity. The parameter n is the inverse of the exponent used in the power law velocity profile, which is often used to model velocity profiles in turbulent flow. For the range of Reynolds numbers in this study, a value of $n = 4$ is applicable.

For fully developed pipe flow, the boundary layer thickness δ is equal to the cylinder inner radius. To effectively transform the flow over a flat plate into flow inside a cylinder, a filter function is applied to the two-wavenumber/frequency spectrum (equation (144)). The filter function is that of a simple linear continuous sensor with a length equal to the inner circumference ($2\pi\delta$) of the cylinder. The integral in spanwise wavenumber of the product of

28

the filter function and the two-wavenumber/frequency spectrum provides a new model of the mode 0 component of the streamwise wavenumber-frequency spectrum and is given as

$$|P_{tbl}(k,\omega_0)|^2 = \int_{-\infty}^{\infty} |P(k,k_2,\omega_0)|^2 \left|\frac{\sin(k_2\pi\delta)}{k_2\pi\delta}\right|^2 dk_2 \ . \tag{150}$$

Figure 8 is a plot of the wavenumber-frequency spectrum of mode 0 in a pipe. The top figure is plotted using a wavenumber range of ±750 rad/m, and the bottom figure is plotted using an expanded wavenumber range of ±5000 rad/m to show the effects of convective ridge energy. The radius of the pipe is 0.00159 m (1/16 in.), the mean flow is 0.535 m/s, the density of the fluid is 1000 kg/m^3, the kinematic viscosity is 1.01 x 10^{-6} m^2/s, and the frequency is 250 Hz. The constant h is 3, b is 0.75, C_T is 0.00467, and C_M is 0.155. The transfer function (equation (150)) in figure 8 is multiplied by 2π to convert the frequency portion of the units from 1/(rad/s) to 1/Hz. Although the energy level of the function reaches a maximum at the convective wavenumber, this energy is filtered out of the system because of the transfer function of the combined fluid and solid structure. The dominant measured effects of the fluid occur between -250 and 250 rad/m, which is the unaliased wavenumber region of the array.
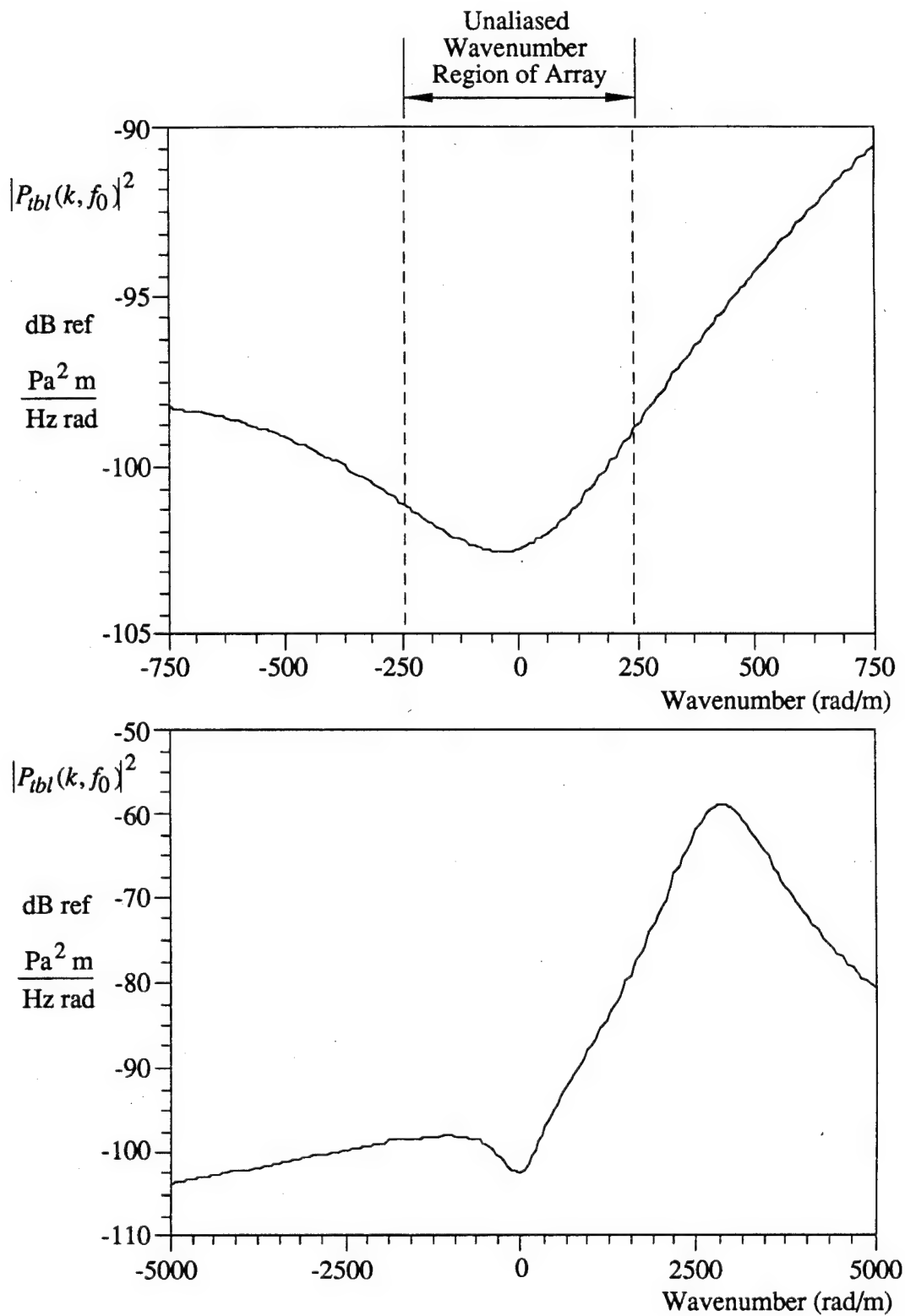
Figure 8. Mode 0 (Axisymmetric) Component of the Wavenumber-Frequency
Spectrum of the Turbulent Wall Pressure Fluctuations

3. EXPERIMENT

The experiment was conducted in an anechoic chamber with the laboratory configuration and array previously described. The data were collected in the time domain using a Labview Data Acquisition system residing on a Macintosh computer. The time domain data were processed as 96 ensemble averages, consisting of 1024-point nonoverlapping fast Fourier transforms, with a Hanning window used for conversion to the frequency domain. The spatial domain data were processed as a 32-point fast Fourier transform, with three zero pads to every one data point. This approach provides a convenient method of interpolating the spatial data in wavenumber.

The surgical tube inner radius (a) is 0.00159 m (1/16 in.), and outer radius (b) is 0.00238 m (3/32 in.). The distance from the middle of the surgical tube to the surface of the urethane (c) is 0.00191 m (3/4 in.). The material properties of the surgical tube and block were measured on a Metravib viscoanalyseur and are listed in tables 1 and 2, respectively. The water had a density of 1000 kg/m^3, a compressional wave speed of 1500 m/s, and a kinematic viscosity of 1.01 x 10^{-6} m^2/s. The four terms of equation (1) were assembled and numerically integrated from -750 to 750 rad/m. Although the limits of integration in equation (1) are from minus infinity to plus infinity, the wavenumber filter rejects most of the high wavenumber energy (e.g., $|k| \geq \omega / u_c$) and thus allows only low wavenumber energy to be passed to the sensors.

Because the measured displacements are extremely small, a reliable method to calibrate the array has not yet been developed. When the theoretical results are compared to the experimental results, the maximum value (in wavenumber) of the theoretical results is matched to the maximum value of the experimental results. Figures 9 to 15 show these results plotted at 100, 150, 200, 250, 300, 350, and 400 Hz, respectively. The theory is plotted with a solid line and the experimental data with X's. The mean flow in the experiment was 0.535 m/s, with a corresponding diameter-based Reynolds number of 1680. Although this is slightly below a fully developed turbulent flow Reynolds number of 2000, it is close to the higher Reynolds

31

number of 1500 that has been observed downstream of stenosis in laboratory experiments (Jones and Fronek, 1988).

Table 1. Material Properties of the Surgical Tube

Frequency (Hz)	Compressional Modulus		Shear Modulus	
	Real (E) N/m^2	Imag (E) N/m^2	Real (G) N/m^2	Imag (G) N/m^2
100	10. x 10^5	1.5 x 10^5	3.4 x 10^5	0.50x 10^5
150	10. x 10^5	1.6 x 10^5	3.4 x 10^5	0.54 x 10^5
200	10. x 10^5	1.7 x 10^5	3.4 x 10^5	0.57 x 10^5
250	10. x 10^5	1.8 x 10^5	3.4 x 10^5	0.60 x 10^5
300	10. x 10^5	1.9 x 10^5	3.4 x 10^5	0.64 x 10^5
350	10. x 10^5	2.0 x 10^5	3.4 x 10^5	0.67 x 10^5
400	10. x 10^5	2.0 x 10^5	3.4 x 10^5	0.67 x 10^5

Table 2. Material Properties of the Urethane

| Frequency (Hz)	Compressional Modulus		Shear Modulus	
	Real (E) N/m^2	Imag (E) N/m^2	Real (G) N/m^2	Imag (G) N/m^2
100	2.1 x 10^5	0.36 x 10^5	0.70 x 10^5	0.12 x 10^5
150	2.1 x 10^5	0.48 x 10^5	0.70 x 10^5	0.16 x 10^5
200	2.1 x 10^5	0.59 x 10^5	0.70 x 10^5	0.20 x 10^5
250	1.9 x 10^5	0.57 x 10^5	0.64 x 10^5	0.19 x 10^5
300	1.9 x 10^5	0.67 x 10^5	0.64 x 10^5	0.22 x 10^5
350	1.8 x 10^5	0.68 x 10^5	0.60 x 10^5	0.23 x 10^5
400	1.7 x 10^5	0.71 x 10^5	0.57 x 10^5	0.24 x 10^5

Figure 9. Theoretical and Experimental Wavenumber Responses at 100 Hz
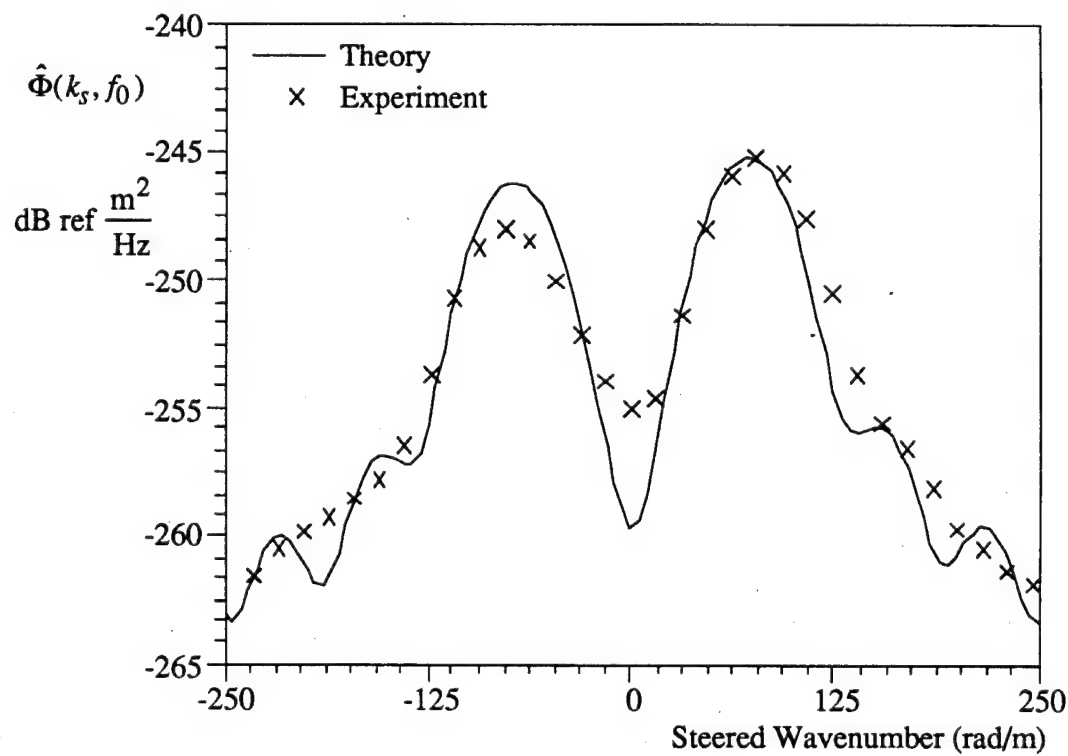

Figure 10. Theoretical and Experimental Wavenumber Responses at 150 Hz
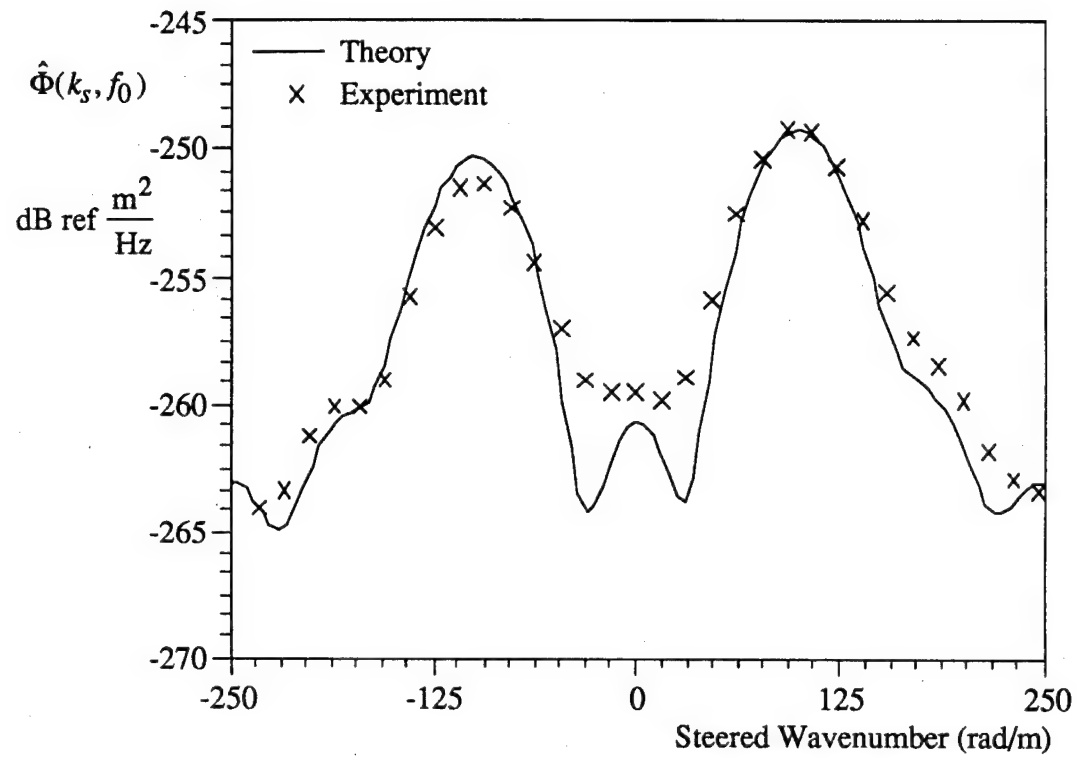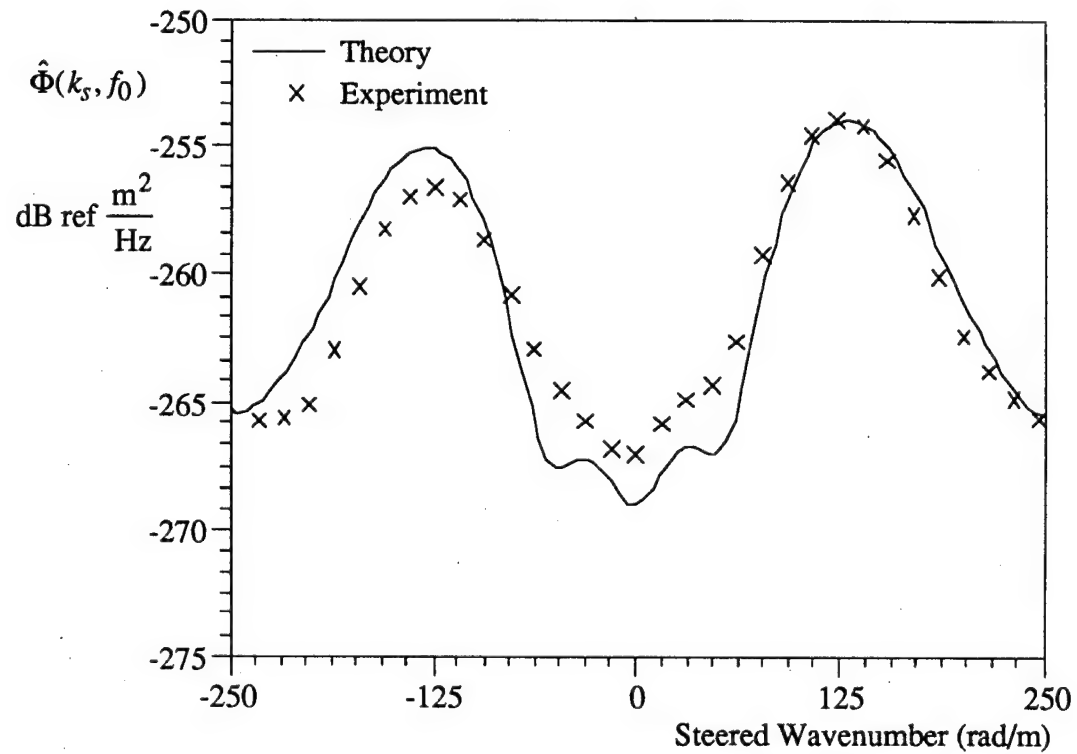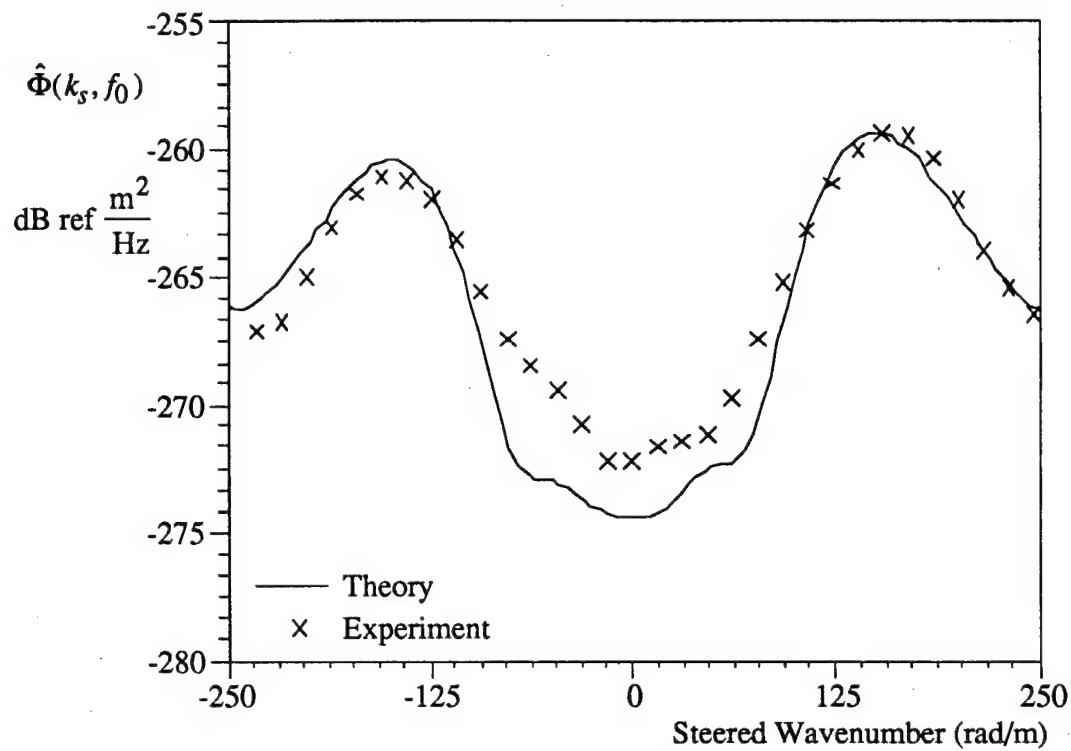
Figure 13. Theoretical and Experimental Wavenumber Responses at 300 Hz
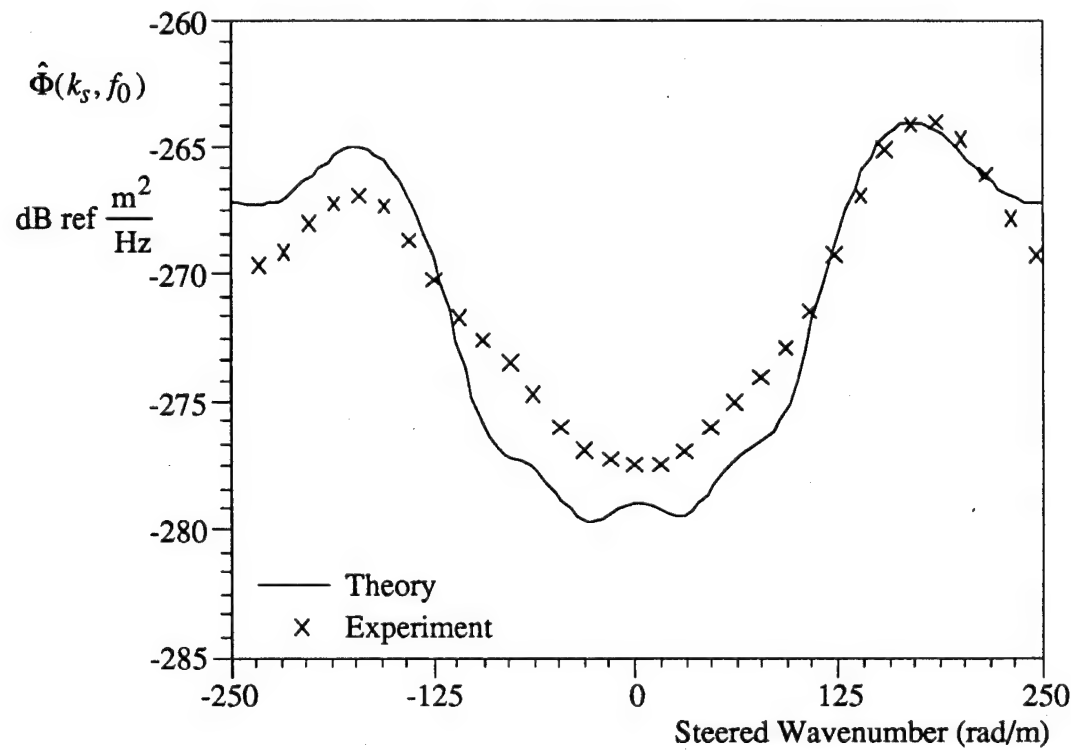
Figure 14. Theoretical and Experimental Wavenumber Responses at 350 Hz

$$\hat{\Phi}(k_s, f_0)$$

dB ref $\dfrac{m^2}{Hz}$
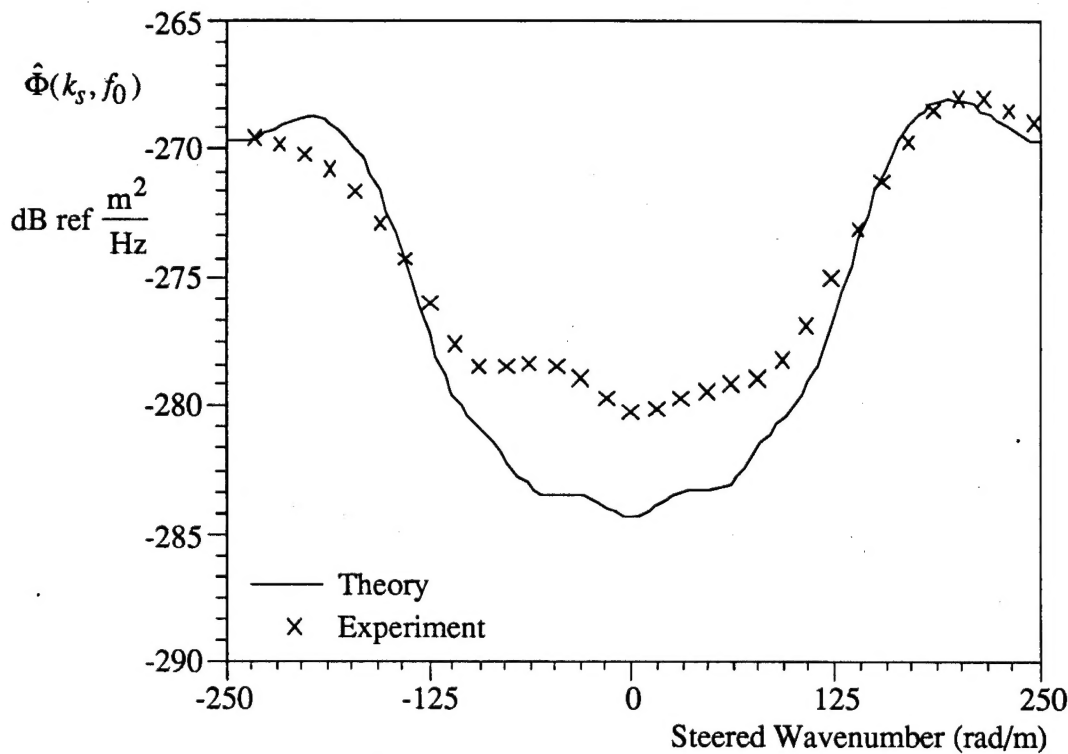
Figure 15. Theoretical and Experimental Wavenumber Responses at 400 Hz

4. DISCUSSION

The turbulent energy present in the embedded tube was measured at the surface of the solid with the array. The energy traveled to the surface by means of a propagating shear wave that originated at the tube wall. The effects of compressional wave motion were small, and these waves did not show up as maxima in the wavenumber cuts. The model was rerun with varying compressional wave speeds that produced results similar to the original results. Changing the stiffness of the embedded tube had a moderate effect on the dynamics of the modeled system. Changing the modeled shear modulus of the embedded tube and/or the solid moved the location of the peaks on the wavenumber plots. This factor must be considered when the array is used to make *in vitro* measurements on human arteries.

The shapes of all the theoretical frequency plots are in relative agreement with the experimental results. The model accurately predicts the shear wave characteristics that are present in the solid. In figures 10, 11, and 12, the magnitude of the near-zero wavenumber regions do not agree exactly in shape, which is probably due to the curved surface assumption used to approximate the flat surface on the urethane block. At low wavenumbers, the wavelengths are long and the effect of surface tension is likely to be more significant than at higher wavenumbers. This magnitude mismatch could also be the result of sensor-to-sensor magnitude and phase mismatch. Additionally, there is some high wavenumber mismatch between the data and the model, which could be due to the phase centers of the elements of the array not being exactly 0.5 inches apart. Slight phase center mismatch will result in experimental results that are shifted slightly in wavenumber.

The source model assumed fully developed turbulent flow in a long pipe and is derived from a flat plate model of the wall pressure spectrum. The accuracy of results based on these premises requires quantification. Effects of transitional (laminar to turbulent) flow, nonhomogeneous tubes (e.g., one with a stenosis), and small radius (curvature) effects should also be examined more closely in further experimentation.

This research illustrates the need to accurately calibrate the sensors. Because the peak value of the measured response was matched to the peak value of the theoretical response, the comparison of the experimental and theoretical results is relative. Although this method provides a good agreement across wavenumber, a better approach would be to make a calibrated measurement and then compare the measured response to the theoretical response.

The wavenumber-frequency beamformer used in this research was extremely accurate in resolving the wavenumber content of the space-time field. However, it is likely that a high resolution (adaptive or optimal) beamformer would provide a better signal processing method to locate spatial sources. Such a beamformer would incorporate the spherical characteristics of the wave and a corresponding loss term.

5. CONCLUSIONS

The space-time field of flow through a long pipe surrounded by an elastic medium was modeled and experimentally verified. A comparison of the model to the experiment showed broad-based agreement in wavenumber and frequency.

6. REFERENCES

Bakewell, H. P., Jr., Carey, G. F., Libuha, J. J., Schloemer, H. H., and Von Winkle, W. A., 1962, "Wall Pressure Correlations in Turbulent Pipe Flow," USL Report No. 559, 1-052-00-00, Underwater Sound Laboratory, New London, CT.

Chase, D. M., 1987, "The Character of the Turbulent Wall Pressure Spectrum at Subconvective Wavenumbers and a Suggested Comprehensive Model," *Journal of Sound and Vibration*, vol. 112(1), pp. 125-147.

Fox, R. W., and McDonald, A. T., 1985, *Introduction to Fluid Mechanics*, John Wiley & Sons, New York.

Jones, S. A., and Fronek, A., 1988, "Effects of Vibration on Steady Flow Downstream of a Stenosis," *Journal of Biomechanics*, vol. 21, no. 11, pp. 903-914.

Norton, C. A., 1995, "A Compilation of Geometric Distance and Tissue Property Data for the Human Thorax," NUWC-NPT Technical Document 11,037, Naval Undersea Warfare Center Detachment, New London, CT.

Potter, M. C., 1978, *Mathematical Methods in the Physical Sciences*, Prentice-Hall, Inc., Englewood Cliffs, NJ.

Timoshenko, S. P., and Goodier, J. N., 1934, *Theory of Elasticity*, McGraw-Hill Book Company, New York.

INITIAL DISTRIBUTION LIST

Addressee	No. of Copies
Analysis and Technology, Inc. (J. Kassal)	5
Defense Technical Information Center	12
Medacoustics Corp. (M. Nixon)	1
Massachusetts General Hospital (R. Levine, MD)	2
Office of Naval Research (ONR 321: T. G. Goldsberry, K. Dial, R. Varley)	3
Structural Acoustics, Inc. (A. Eberhardt (2), C. Chassaing (2))	4